Nature Communications

https://doi.org/10.1038/s41467-026-69582-y

Article in Press

A pulsed optoelectronic microwave source with high power and frequency tunability

Received: 30 July 2025

Accepted: 29 January 2026

Cite this article as: Niu, X., Wang, L., Zhang, B. *et al.* A pulsed optoelectronic microwave source with high power and frequency tunability. *Nat Commun* (2026). https://doi.org/10.1038/s41467-026-69582-y

Xinyue Niu, Langning Wang, Bin Zhang, Junpu Ling, Qian Zhang, Muyu Yi, Jinmei Yao, Jing Hou, Hanwu Yang, Xiaotao Xu, Bo Jiang, Juntao He, Jinliang Liu, Jiande Zhang, Hui Jing, Tao Xun & Jun Zhang

A pulsed optoelectronic microwave source with high power and frequency tunability

Xinyue Niu [1,†], PhD; Langning Wang [1,2,†], PhD; Bin Zhang [1,2], PhD; Junpu Ling [1,2], PhD; Qian Zhang [3], PhD; Muyu Yi [1,2], PhD; Jinmei Yao [1,2], PhD; Jing Hou [1,2], PhD; Hanwu Yang [1,2], PhD; Xiaotao Xu [4], PhD; Bo Jiang [1,2], PhD; Juntao He [1,2], PhD; Jinliang Liu [1,2], PhD; Jiande Zhang [1,2], PhD; Hui Jing [5], PhD; Tao Xun [1,2,*], PhD; Jun Zhang [1,2,*] PhD

† These authors contributed equally to this work

[1]College of Advanced Interdisciplinary Studies, National University of Defense Technology, Changsha 410073, China

[2]Nanhu Laser Laboratory, National University of Defense Technology, Changsha 410073, China

[3]Department of Physics and Synergetic Innovation Center for Quantum Effects and Applications, Hunan Normal University, Changsha 410073, China

[4]Information Support Force Engineering University, Wuhan, 430035, China

[5]College of Science, National University of Defense Technology, Changsha 410073, China

Corresponding author: Jun Zhang

E-mail: zhangjun_nudt@126.com

Co-corresponding author: Tao Xun

Tel.: +86 13607488836 , **E-mail:** xuntao@nudt.edu.cn

Abstract

Microwave sources are central to modern technologies ranging from radar and directed energy to medical applications, yet conventional electronic approaches face long-standing trade-offs between output power and tunability. Optoelectronic techniques offer a promising alternative by combining the broad bandwidth of optical systems with the high power-handling capability of wide-bandgap semiconductors**.** Here we show an optoelectronic microwave source based on fast-response silicon carbide, enabling picosecond-scale control of photogenerated carrier lifetime while sustaining power-handling capacities up to 55 MW. The system generates continuously tunable pulsed microwave emission across the P–L band, delivering peak output power exceeding 1 MW over the 0.25–1.3 GHz range and exhibiting stable nanosecond-scale pulse operation. The generated pulses exhibit low timing jitter and highly efficient power combining in array operation. These results demonstrate a scalable route toward high-power, broadband, and flexible microwave sources, enabling applications that demand simultaneous control over frequency, energy, and spatial distribution.

Key words: high-power microwave (HPM); optoelectronic microwave system (OEMS); wide-bandgap (WBG) photoconductive semiconductor device (PCSD); multi-parameter adjustable microwave generation; multi-channel power synthesis

1. INTRODUCTION

High-power microwave (HPM) sources are crucial for applications in directed energy [1], detection and localization [1, 2], particle acceleration [15], medical treatments [3, 4], microwave heating [5–7], and plasma generation [8, 9]. Among these, detection, localization, and directed-energy applications impose strict requirements on the operating bandwidth and frequency agility of microwave sources to accommodate multi-band demands such as radio communication (~0.4–1 GHz), Wi-Fi (2.4 GHz), GPS (1.5 GHz), airborne navigation, and satellite links within the L-band. Multi-frequency microwave heating and plasma sources provide significantly improved heating performance and control flexibility compared to fixed-frequency methods. Similarly, high-intensity, tunable pulsed electric fields (PEFs) offer emerging strategies for tumor ablation. Consequently, the development of waveform-modulation and radiation technologies that simultaneously provide wide bandwidth and high power has become a critical focus in microwave research, enabling multifunctional system integration, enhanced operational effectiveness, and expanded application targets [10–13] (Fig. 1f).

Purely electronic microwave sources include vacuum and solid-state types, with vacuum electronic devices (VEDs) and solid-state power amplifiers (SSPAs) as core components (Fig. 1a). VEDs convert electron beam kinetic energy into microwave energy via beam–wave interaction, achieving gigawatt-level peak powers and Ka-band frequencies [14], [15]. However, the center frequency, dictated by the slow-wave structure (SWS), restricts their adaptability across scenarios and targets [16], [17]. Traveling wave tubes (TWTs), a subset of VEDs, offer limited tunability, with relative bandwidths up to 77% [18–21]. Yet, backward-wave oscillations and thermal issues limit their peak power to ~10 kW [22], [23]. Overall, their single-frequency output and bulky size make VEDs ill-suited for integrated, multifunctional P–L-band applications.

To enhance flexibility, SSPAs have been used to achieve frequency-tunable outputs [24], [25]. SSPAs tune microwave frequency via gate-controlled carrier modulation. In particular, high electron mobility transistors (HEMTs), based on two-dimensional electron gases (2DEGs) (Fig. 1a), offer faster response than traditional metal–oxide–semiconductor field-effect transistors (MOSFETs). However, single HEMT devices are limited to kilowatt-level power, with maximum relative bandwidths of 10% (kW-level) and 40% (100-W-level) [26–32]. Compared with purely electronic approaches (Fig. 1b), the optoelectronic method provides broader frequency coverage and greater tunability while maintaining megawatt-level peak power [33–38].

Here, we show a high-power microwave source based on optoelectronic technology (Fig. 1c). The overall architecture of the optoelectronic microwave source (OEMS) is described, followed by an explanation of its submodules, including fast-response materials, high-voltage-resistant devices, and high-power system

components. Finally, the application of the array configuration is discussed. The OEMS demonstrates higher frequency–peak-power performance than traditional electronic microwave sources (Fig. 1d). Moreover, in optoelectronic systems, the photoconductive semiconductor architecture of the OEMS mitigates the limitations on source–drain spacing and output power imposed by carrier transit time, thereby enabling higher output power (Fig. 1e). A detailed comparison of performance metrics is provided in Supplementary Note 19.

2. RESULTS

2.1. Overall Architecture of the OEMS

In contrast to sub-nanosecond pulse sources relying on nonlinear photoconductive mechanisms, which suffer from limited operational flexibility [S22–S26], this study adopts a linear photoconductive strategy, wherein the core principle is to amplify radio-frequency signals via an electrical–optical–electrical conversion pathway. The conceptual schematic and overall architecture of the OEMS are illustrated in Fig. 2a,b. GHz-range microwave output is achieved through a combination of optical modulation, amplification, optoelectronic conversion, and array-based radiation. The laser source employs a master oscillator power amplifier (MOPA) architecture, wherein a modulated seed converts weak electrical signals into tunable optical pulses. A narrowband laser diode (LD) generates the initial pulsed beam, followed by preamplification to enhance the initial power level. An electro-optic modulator (EOM) applies GHz-range modulation, accurately imprinting the RF signal onto the optical carrier with support for a dynamic bandwidth of up to 10 GHz. A subsequent acousto-optic modulator (AOM) tailors the temporal envelope, enabling tunable repetition rates from 10 Hz to 10 kHz and pulse durations ranging from sub-nanoseconds to 1 μs [39]. Together, these components generate a clean and reconfigurable seed pulse, enabling precise control over the center frequency, pulse width, and repetition rate of the OEMS output.

The seed pulses subsequently undergo multi-stage fiber amplification (AMP-1/2/3), employing polarization-maintaining, highly doped fibers with progressively increasing core diameters to boost peak output power. A Pockels cell–based repetition-rate reducer ensures synchronization and polarization stability. Final amplification is conducted via a cascaded Nd:YAG solid-state stage, pulse-pumped to generate high-energy pulse clusters. The amplified optical pulses are coupled into a power-delivery fiber and distributed across multiple photoconductive channels.

The system circuitry can be modeled as a series network comprising a high-voltage supply, an energy storage capacitor, a photoconductive semiconductor device (PCSD), and an output load. Detailed material and device designs of the PCSD are presented in the following sections. An RF transmission structure located at the device output delivers microwave power to the load. A suspended-plate antenna array is integrated at the terminal stage,

powered and monitored by a custom constant-current voltage source to enable multi-channel radiation. A detailed schematic of the full system layout is available in Supplementary Note 1.

When the incident laser modulates the material resistance (R_{SiC}), it alters the voltage division between R_{SiC} and R_{load}, thereby inducing a variation in the load voltage and generating high-power GHz-range RF signals. Equation (1) captures the relationship among the material resistanceR_{SiC}, substrate thickness d, electrode area S_0, and photo-generated carrier concentration $n(t)$, whereas Equation (2) describes the relation between the output voltage V_{out} and the bias voltage V_{bias}. Detailed derivations and symbol definitions are provided in Supplementary Note 2.

$$R_{SiC}(t) = \frac{d}{n(t) q \mu_n S_0} = \frac{d^2 h\nu (1 - Re^{-2\alpha d})}{q\mu_{\mathrm{n}} \eta (1-R)(1-e^{-2\alpha d}) \int_{-\infty}^{t} P(s) e^{(s-t)/\tau_0} ds} \tag{1}$$

$$V_{out} = V_{bias} \cdot \sqrt{\Phi_{structure}(f)} \approx V_{bias} \cdot \frac{R_{load}}{R_{load} + R_{SiC}} \tag{2}$$

2.2. Fast-Response Materials for OEMS

The wide-bandgap semiconductor SiC is employed due to its favorable properties, enabling exceptional performance in high-voltage and high-temperature environments [40–42]. For photogenerated carriers, both their generation and capture are essential to achieving high power and fast response [43]. By adopting a shallow donor-deep acceptor (SDDA) complementary doping scheme, shallow energy levels (Nitrogen, Ec-0.05~0.09 eV) ionize electrons in the dark state, which are then captured by traps to maintain high insulation (Supplementary Note 3). Upon exposure to extrinsic light (1064 nm), electrons trapped in deep acceptor levels (Vanadium, Ec-0.81~0.97 eV) transition to the conduction band, generating free carriers (Fig. 3a). The material's optical absorption depth is on the millimeter scale [44], [45], ensuring conduction between the electrodes.

To maximize OEMS output in the P–L band, the total response time is designed to fall between 100 and 150 ps (Fig. 3b). In the photodiode mechanism [46-49], the total response time is given by $\tau_{total} \approx \sqrt{\tau_{tr}^{\ 2} + \tau_{RC}^{\ 2}}$,where τ_{tr} and τ_{RC} denote the carrier transit time through the depletion region and the circuit response time, respectively. In comparison, the total response time of the OEMS is determined by $\tau_{total} \approx \sqrt{\tau_0^{\ 2} + \tau_{RC}^{\ 2}}$, where τ_0 represents the carrier lifetime. With an interstage capacitance of 1.6 pF and an N/V doping ratio of 0.4, both the circuit response time and carrier lifetime are approximately 80 ps, yielding a total response time of 113 ps. For millimeter-scale dimensions, the OEMS exhibits a total response time approximately 1% that of the photodiode (Fig. 3c). As previously noted, the OEMS overcomes the trade-off between material thickness and response frequency, making it well suited high-frequency response in millimeter-

scale devices.

Carrier lifetime was tested for two designed substrate samples, Sample 1 and Sample 2 (Supplementary Note 4). The capture times of the V acceptor level for the two samples were 8.4 ps and 80.2 ps, respectively (Fig. 3d). The OEMS incorporating Sample 2 exhibited predicted voltage responses of 100% and 50% at laser frequencies of 0.25 GHz and 2.5 GHz, respectively (Fig. 3e). Sample 1 is predicted to extend frequency response up to 10 GHz; however, output amplitude would decrease markedly, and planar electrodes should be used to reduce capacitance.

Furthermore, several strategies can effectively facilitate frequency extension in regimes with short carrier lifetimes. First, optimizing doping levels and introducing efficient recombination centers enhance transient photoconductivity and improve high-frequency response. At a fixed concentration, recombination centers with larger electron capture cross-sections can enhance the device's high-frequency performance (Fig. 3f). Second, device design should simultaneously increase the overall doping concentration to reduce conduction resistance and minimize load impedance, thereby enhancing power output (Fig. 3g). Finally, optimizing the external electrode layout and RF transmission pathway can further extend the circuit bandwidth into higher frequency regimes [50, 51]. Further technical details are provided in Supplementary Note 5.

2.3. High-Voltage and High-Current Devices for OEMS

A device with opposing electrodes has been developed (Fig. 4a), in which the laser is incident through a transparent electrode into the substrate. Compared to planar electrodes, this configuration prevents surface flashover breakdown, offering advantages in blocking voltage and operational lifetime. To mitigate collision ionization induced by high current density, the incident light is confined to a low-field region away from the electrode edges. Consequently, during device operation, the peak electric field and peak current density do not coincide, as shown in Fig. 4b. The dark-state breakdown voltage of the 0.5 mm vertical device was tested (Supplementary Note 6), with breakdown occurring at the electrode edge when the bias voltage reached 46 kV (Fig. 4c).

The optical coupling structure is illustrated in Fig. 4d. A comparison was conducted between a single-reflection configuration and a short-cavity, multiple-pass design employing total internal reflection (Supplementary Note 7). For a cavity length of 10 mm, the total-internal-reflection scheme enhances optical intensity by a factor of 3.5 relative to single reflection. However, the associated round-trip delay of 170 ps introduces group delay dispersion and potential saturation, thereby limiting the high-frequency response. Given the OEMS's emphasis on broadband performance and waveform fidelity, the single-reflection configuration was selected. An AZO layer (150 nm thick), deposited on the front surface of the SiC substrate, yields a theoretical

optical coupling efficiency of 98%, with an experimentally measured value of 95% (Fig. 4e). Under a substrate thickness of 1.5 mm and an N/V doping ratio of 0.4 (1×10^{17} / 2.5×10^{17} cm^{-3}), the average optical absorption is approximately 23% (Fig. 4f).

The output peak currents under varying bias voltages and light intensities are shown in Fig. 4g. The output amplitude increases linearly with bias voltage (1–3 kV) and approximately proportionally with incident light intensity (0.1–34 mJ). Simulation results indicate that, when triggered by a single-pulse laser with 35 mJ energy and a 7 ns pulse width, the device reaches a minimum on-resistance of 5.3 Ω (Supplementary Note 8). Finally, the conduction current under illumination was measured with a bias voltage of 30 kV and a circuit load of 11.3 Ω. The results show a maximum conduction current of 1.86 kA, with a power capacity of 55 MW and a minimum on-resistance of 4.83 Ω (Fig. 4h), positioning the PCSD among high-performance photoconductive devices (Fig. 4i).

2.4. Integrated Performance of the OEMS

The coaxial tapered structure provides a 3 dB bandwidth of 0–3 GHz (Supplementary Note 9), enabling low-loss RF power transmission within the PCSD. Fig. 5a displays the time-domain output waveforms of the OEMS. At a bias voltage of 22 kV and a trigger energy of 30 mJ (Supplementary Note 10), the 1 GHz microwave pulse achieves a peak power of 1.36 MW and an intra-pulse average power of 0.68 MW (Supplementary Note 11). The pulse width is 30 ns, with a repetition rate of 100 Hz. As shown in Fig. 5b, the peak power decreases with increasing frequency, primarily constrained by the overall response time of the OEMS. Overall, the OEMS achieves megawatt-level peak power while offering continuous and flexible frequency tunability across the P–L band, fulfilling the demands of high-power, multi-parameter microwave systems.

To evaluate the spectral purity of the generated microwave pulses, the FFT-derived power spectrum is shown in Fig. 5c. Harmonic components are suppressed by more than −14 dB relative to the fundamental frequency, and the measured 3 dB bandwidth of the main spectral line is 27 MHz, consistent with the 30 ns pulse width (Supplementary Note 12). A slight waveform broadening caused by voltage division within the series circuit is identified as the primary source of second-harmonic content. These harmonics contribute negligibly to the peak power, ensuring that the actual power at the target frequency closely matches the value calculated using the voltage-based method.

At megawatt output levels, potential sources of harmonic or nonlinear contributions include the voltage-division network, carrier dynamics in the material, parasitic circuit elements, and optical/electrical saturation effects. Among these, series load division is currently the most probable origin of harmonic generation. Material doping and device-level parasitics may introduce frequency-dependent nonlinearities in the output voltage.

Additionally, when the incident optical energy exceeds 12 mJ within a 10 ns pulse and the bias field surpasses 30 kV/mm, nonlinear phenomena such as optical saturation and carrier velocity saturation are expected to become prominent. In the current OEMS system, however, both the optical power and electric field strength operate within the linear regime. Detailed saturation thresholds are provided in Supplementary Note 13.

2.5. Array Application of the OEMS

In large-scale array power synthesis, the standard deviation of time jitter is a critical performance metric and is determined by the stability of the trigger laser. To achieve synthesis efficiency above 95% at 2 GHz, the time jitter must remain below 20 ps (Supplementary Note 15). The 2 GHz optical signal was characterized within an 8 ns amplitude-flat region (Fig. 6a). As shown in Fig. 6b, at an optical energy of 24 mJ, the time jitter of the optical signal is 11 ps, meeting the phase-control requirements for efficient array synthesis. By applying an FFT to the absolute time-jitter sequence, the modified phase-noise power spectrum over the (0, 2 GHz] range was obtained (Supplementary Note 16), and the relationship is expressed as $\sigma_{abs}{}^2 = 1/w_0{}^2 \int_0^{f_0} 2L(f)df$. As shown in Fig. 6c, periodic spurious peaks introduced by the measurement window appear at 120 MHz and its harmonics, while the noise spectrum exhibits <−85 dBc/Hz near 87 MHz. This noise is attributed to active-device noise within the optical amplification chain and trigger jitter from the synchronized driving signals. Future work will focus on reducing phase noise within the sub-100 MHz region.

The measurement setup is shown in Fig. 6d (Supplementary Note 14). When the four elements radiated sequentially, the average far-field amplitudes were 257.9 mV, 253.9 mV, 239.2 mV, and 256.7 mV, respectively. When radiating simultaneously, the array produced an average far-field amplitude of 1.02 V (Fig. 6e), corresponding to a spatial synthesis efficiency of 98.6%. The amplitude stability of the single-path and array-combined signals was better than ±9.5% and ±7.36%, respectively (Supplementary Note 17). In addition, the measured radiation pattern gain closely agrees with the simulation results (Fig. 6f). These results demonstrate that the OEMS not only offers modularity, compactness, and tunable-frequency waveform generation, but also achieves high-efficiency, high-power array synthesis, thereby enabling the development of integrated, multifunctional microwave systems.

3. DISCUSSION

This study presents an approach for generating high-power microwaves by leveraging wide-bandgap semiconductors and the broadband advantages of optics. It addresses the limitations of traditional vacuum electronic devices and solid-state power amplifiers, where balancing peak power and frequency tunability is inherently challenging. Design requirements at the material, device, and system levels were analyzed. The trade-off between efficient excitation and rapid recombination in the material was addressed, along with challenges in

high-voltage device design and efficient RF transmission. As a result, the OEMS generates MW-level peak-power microwave pulses over the 0.25–1.3 GHz range with continuous frequency tunability within the P–L band; the pulses have a 30-ns FWHM duration at a pulse-repetition frequency of 100 Hz. Building on this, a microwave power synthesis array achieving 98.62% efficiency was constructed, demonstrating flexible scalability in energy, spatial, and frequency domains for integrated, miniaturized applications.

The system described here is designed to demonstrate its maximum instantaneous output capability and, as such, operates in pulsed mode. Adaptation to continuous-wave (CW) operation can be achieved by reconfiguring the optical source. By replacing the pulsed LD with a CW laser, the MOPA-based architecture can generate stable continuous microwave output (Supplementary Note 18). Although the maximum power in CW mode is lower than in pulsed operation, power scaling can still be achieved through multi-channel synthesis, thus enabling broader application potential.

4. METHODS

4.1. Device Configuration and Fabrication

The 4H-SiC material was selected with an optimized nitrogen/vanadium (N/V) doping ratio of 0.4 (1×10^{17} / 2.5×10^{17} cm^{-3}). The wafer was cut along the a-plane ($11\bar{2}0$-plane) to eliminate micropipes, from which a substrate measuring 8 mm × 8 mm with a thickness of 1.5 mm was obtained. The photoconductive device consists of the substrate, electrodes, and an optical coupling structure. A face-to-face electrode configuration is employed on both sides of the substrate, consisting of an annular multilayer metal electrode (Ti/Ni/Au with respective thicknesses of 30 nm, 80 nm, and 100 nm, patterned by photolithography) and a circular transparent electrode. The outer diameters of the metal and transparent electrodes are 3.5 mm and 2 mm, respectively. The bilayer electrode structure is annealed at 900 °C for 2 minutes to ensure a reliable ohmic contact. The transparent electrode is composed of aluminum-doped zinc oxide (Al:ZnO, AZO), with a thickness of 150 nm, selected based on thin-film interference considerations to enhance the transmittance of normally incident laser light. The bottom AZO layer is heavily doped to reduce the space-charge region at the AZO/SiC junction, thereby lowering the conduction resistance [S27]. In the axial illumination configuration, the two electrodes are directly aligned, yielding an effective illuminated area of 9.62 mm^2 and an interstage capacitance of approximately 1.8 pF. To optimize optical efficiency, the incident laser beam is collimated to minimize divergence loss, and a single-reflection scheme incorporating a terminal mirror is used to improve optical energy utilization. After encapsulation, the overall dimensions of the photoconductive semiconductor device (PCSD) are approximately $2 \times 2 \times 3$ cm^3.

4.2. PCSD Testing Setup

The test circuit used for dark DC breakdown measurements consists of a SiC substrate with a pair of opposing electrodes, with a substrate thickness of 0.5 mm. A 1:5 closed-loop magnetic voltage transformer (XF) is employed, and the high-voltage power supply is charged through a ceramic energy-storage capacitor (C1, 50 kV, 2 nF). The voltage across the device under test is monitored using a high-voltage probe.

The circuit used for evaluating the power capacity of the PCSD includes six 40 kV, 1 nF ceramic capacitors connected in parallel, six 50 Ω resistors, and a current-viewing resistor (CVR). During the photoconductive switch test, the ceramic capacitor bank charges the high-voltage supply. Upon laser triggering, the capacitor discharges through the device, which is modeled as a variable resistor. The CVR serves as a low-value, high-bandwidth resistor (2 GHz; T&M SSDN-10, New Mexico, USA). The output signal is recorded using a 4 GHz bandwidth oscilloscope (LeCroy WR9404M, New York, USA). A 1064 nm Nd:YAG laser with a 7 ns pulse width and a 2 mm beam diameter is used for excitation.

4.3. Array Synthesis Testing Setup

Time interval error (TIE) is used to quantify time jitter, with its standard deviation computed from 1×10^4 data points. Approximately 50 peak amplitudes are recorded to evaluate amplitude fluctuations. The pulsed laser is collimated, expanded, and split into five paths; four illuminate the photoconductive devices, and one is used for real-time intensity monitoring. The PCSD is connected to the high-voltage supply at the input and to a suspended plate antenna at the output through an L29 connector. Far-field measurements are performed at 1.37 m at 1.3 GHz. The transmitting and receiving antenna gains are 15.5 dB and 7.15 dB, respectively. After 40 dB and 20 dB attenuation, the signal is delivered to the oscilloscope via a 20 m SMA cable, resulting in a total link attenuation of ~83.01 dB. Array synthesis efficiency is obtained from the average far-field amplitude over more than 50 repeated measurements.

Data availability:

The source data generated in this study have been deposited in the Figshare database under accession code https://doi.org/10.6084/m9.figshare.30963374.

Code availability: All codes used in this study are available from the corresponding authors upon request.

REFERENCES

1. Rumelhard, C., Algani, C., Billabert, A. L. Microwaves Photonic Links: Components and Circuits. (John Wiley & Sons, Inc., Hoboken, NJ, 2017).
2. Andreas, B. et al. Lithium niobate photonics: unlocking the electromagnetic spectrum. *Science* **379**, 40 (2023).

3. Casciati, A. et al. Effects of ultra-short pulsed electric field exposure on glioblastoma cells. *Int. J. Mol. Sci.* **23**, 3001 (2022).
4. Karunasagara, S. et al. Electrically-stimulated cellular and tissue events are coordinated through ion channel-mediated calcium influx and chromatin modifications across the cytosol-nucleus space. *Biomaterials* **314**, 122854 (2025).
5. Wang, S. et al. Modeling and simulation of a multi-source microwave heating of soil based on PSO-BPNN. *Appl. Therm. Eng.* **257**, 124148 (2024).
6. Yang, B. et al. The optimization of consensus decision-making for a multi-microwave source system based on composite leader-follower clustering for intelligent agent-based joint heating temperature field. *Case Stud. Therm. Eng.* **66**, 105668 (2025).
7. Yang, R., Chen, J. Heating performance of dual-source microwave heating using different frequency shifting strategies in a solid-state system. *Food Res. Int.* **175**, 113781 (2024).
8. Chen, C. et al. Dual-frequency microwave plasma source based on microwave coaxial transmission line. *Appl. Sci.* **11**, 9873 (2021).
9. Sekiguchi, H. Experimental investigations of plasma-assisted ammonia combustion using rod-electrode-type microwave plasma source. *Int. J. Hydrog. Energy* **65**, 66–73 (2024).
10. Seeds, A. J., Williams, K. J. Microwave photonics. *J. Lightwave Technol.* **24**, 4628–4641 (2006).
11. Yao, J. Arbitrary waveform generation. *Nat. Photonics* **4**, 79–80 (2010).
12. Hui, X., Kan, E. C. Radio ranging with ultrahigh resolution using a harmonic radio-frequency identification system. *Nat. Electron.* **2**, 125–131 (2019).
13. Zhu, X. et al. Agile manipulation of the time-frequency distribution of high-speed electromagnetic waves. *Nat. Commun.* **15**, 8942 (2024).
14. Li, X. et al. Meta-surface-assisted high-power broadband rectangular $TE_{1,0}$ mode window for vacuum electronic devices. *IEEE Trans. Microw. Theory Tech.* 1–7 (2025).
15. Guo, G. et al. Investigation and batch fabrication of G-band broadband and low-loss monocrystalline diamond window for vacuum electron devices. *IEEE Electron Device Lett.* **45,** 1981–1984 (2024).
16. Zhang, J. et al. Research progresses on cherenkov and transit-time high-power microwave sources at NUDT. *Matter Radiat. Extremes* **1**, 163–178 (2016).
17. James, B., Edl, S., Coty, S. J., A., S. J. & Peng, Z. High Power Microwaves. (Taylor & Francis Group, Abingdon, 2024).
18. Ayllon, N. Microwave high power amplifier technologies for spaceborne applications. *IEEE 16th Annual Wireless and Microwave Technology Conference (WAMICON)*, Cocoa Beach, FL, USA (2015).
19. Prakash, D. J. et al. Self-winding helices as slow-wave structures for sub-millimeter traveling-wave tubes. *ACS Nano* **15,** 1229–1239 (2021).

20. Wang, Y. et al. Electro-thermal co-simulation of high-frequency structure of staggered double-grating traveling wave tube based on finite difference time domain. *Case Stud. Therm. Eng.* **61**, 104833 (2024).
21. Sharma, R. et al. Power characteristics of a high-performance helix traveling wave tube. *Case Stud. Therm. Eng.* **56**, 104199 (2024).
22. Trubetskov, D. I. & Vdovina, G. M. Traveling wave tubes: a history of people and fates. *Phys. Uspekhi* **63**, 1–13 (2020).
23. Wu, G. et al. Theory and hot test of high-power broadband helix traveling-wave tube based on a double-graded radius and pitch circuit. *IEEE Electron Device Lett.* **42,** 1868–1870 (2021).
24. Qiu, C. et al. Dirac-source field-effect transistors as energy-efficient, high-performance electronic switches. *Sci. Found. China* **361**, 387–392 (2018).
25. Guo, S. et al. Ultrascaled double-gate monolayer SnS_2 MOSFETs for high-performance and low-power applications. *Phys. Rev. Appl.* **14**, 044031 (2020).
26. D'Ambrosio, R. et al. Improved densification of SiC_f/SiC composites by microwave-assisted chemical vapor infiltration process based on multifrequency solid-state sources excitation. *J. Eur. Ceram. Soc.* **45**, 116950 (2025).
27. Rayrat, G. et al. A new sinter-forging process based on a 915 MHz solid-state microwave source for sintering of oxide ceramics. *J. Eur. Ceram. Soc.* **45**, 117262 (2025).
28. Jing, X. D. et al. A 150-W spaceborne GaN solid-state power amplifier for Beidou navigation satellite system. *IEEE Trans. Aerosp. Electron. Syst.* **58**, 2383–2393 (2022).
29. Giofre, R. et al. Design realization and tests of a space-borne GaN solid-state power amplifier for second generation Galileo navigation system. *IEEE Trans. Aerosp. Electron. Syst.* **54**, 2383–2396 (2018).
30. Naderi, P., Fallahi, F. A design strategy for bandwidth enhancement in three-stage Doherty power amplifier with extended dynamic range. *IEEE Trans. Microw. Theory Tech.* **66**, 1024–1033 (2018).
31. Zhou, H. et al. A generic theory for design of efficient three-stage Doherty power amplifiers. *IEEE Trans. Microw. Theory Tech.* **70**, 1242–1253 (2022).
32. Xia, J. et al. Improved three-stage Doherty amplifier design with impedance compensation in load combiner for broadband applications. *IEEE Trans. Microw. Theory Tech.* **67**, 778–786 (2019).
33. De Chatellus, H. G. et al. Reconfigurable photonic generation of broadband chirped waveforms using a single CW laser and low-frequency electronics. *Nat. Commun.* **9,** 1–12 (2018).
34. Cohen, L. M. et al. Silicon photonic microresonator-based high-resolution line-by-line pulse shaping. *Nat. Commun.* **15**, 7878 (2024).
35. Supradeepa, V. R. et al. Comb-based radiofrequency photonic filters with rapid tunability and high selectivity. *Nat. Photon.* **6**, 186–194 (2012).
36. Xie, X. et al. Photonic microwave signals with zeptosecond-level absolute timing noise. *Nat. Photon.* **11**, 44–47 (2017).

37. Jiang, H. et al. Simultaneous achieving negative photoconductivity response and volatile resistive switching in Cs2CoCl4 single crystals towards artificial optoelectronic synapse. *Light: Sci. Appl.* **13**, 316 (2024).

38. Capmany, J., Novak, D. Microwave photonics combines two worlds. *Nat. Photon.* **1**, 319–330 (2007).

39. Gu, Y. et al. High-power microsecond ultraviolet burst-mode pulse laser with a rectangular envelope and GHz-adjustable intra-burst pulses. *High Power Laser Sci. Eng.* **13**, e23 (2025).

40. Fang, J. et al. Electron transport properties of $Al_xGa_{1-x}N$/GaN transistors based on first-principles calculations and Boltzmann-equation Monte Carlo simulations. *Phys. Rev. Appl.* **11**, 044045 (2019).

41. Zhang, Y. et al. Highly sensitive photoelectric detection and imaging enhanced by the pyro-phototronic effect based on a photoinduced dynamic Schottky effect in 4H-SiC. *Adv. Mater.* **34**, 2204363 (2022).

42. Choi, S. H. et al. Heterogeneous integration of wide bandgap semiconductors and 2D materials: Processes, applications, and perspectives. *Adv. Mater.* **37**, 2411108 (2024).

43. Wang, S. J. et al. Highly efficient modulation doping: a path toward superior organic thermoelectric devices. *Sci. Adv.* **8**, 9264 (2022).

44. Xun, T. et al. Recent progress of parameter-adjustable high-power photonic microwave generation based on wide-bandgap photoconductive semiconductors. *Chin. Opt. Lett.* **22**, 118–127 (2024).

45. He, T. et al. Effect of donor–acceptor compensation on transient performance of vanadium-doped SiC photoconductive switches using 532-nm laser. *IEEE Trans. Electron Devices* **71**, 1–8 (2024).

46. Najarian, A. M. et al. Photophysical properties of materials for high-speed photodetection. *Nat. Rev. Phys.* **6**, 219–230 (2024).

47. Franklyn, Q. The photodetection of ultrashort optical pulse trains for low noise microwave signal generation. *Laser Photonics Rev.* **17**, 1 (2023).

48. Petter, L., Heck, M. J. R. High-power microwave generation through distributed optical amplification into a photodiode array on an open indium phosphide platform. *J. Lightwave Technol.* **38**, 5526–5535 (2020).

49. Keye, S., Andreas, B. High-speed photodetectors for microwave photonics. *Appl. Sci.* **9**, 623 (2019).

50. Zeng, L. et al. Dual-stacked SiC vertical photoconductive switch for modulation bandwidth extension of frequency-agile power microwave. *IEEE Electron Device Lett.* **45**, 992–995 (2024).

51. Chu, X. et al. Wide-range frequency-agile microwave generation up to 10 GHz based on vanadium-compensated 4H-SiC photoconductive semiconductor switch. *IEEE Electron Device Lett.* **43**, 1 (2022).

Acknowledgments

The work was supported in part by the National Key R\&D Program (Grant No. 2024YFE0102400, awarded to H.

J.), a Key Program of the National Natural Science Foundation of China (Grant No. 62434010, awarded to T. X.), a National Natural Science Foundation of China (Grant No: 62101577, awarded to T. X.), and a grant from the Natural Science Foundation of Hunan Province (Grant No: 2021JJ40660, awarded to T. X.). We would like to thank Dr. Yanran Gu and Dr. Ting He for the sincere help and support on the fabrication and test.

Author Contributions: T. X., L. W., and Jun Z. conceived the idea of using linear control of photonic semiconductors to generate high-power microwaves. X. N., H. Y., and Jiande Z. contributed to the theoretical simulation models. B. Z., Jing H., and J. Y. developed the laser source platform. X. N., M. Y., and Junpu L. were responsible for the system link setup and testing. X. N., H. J., and Q. Z. drafted the main sections of the manuscript. Jinliang L. and Jiande Z. contributed to the data processing and analysis. B. J., Juntao H., and X. X. coordinated the experimental instruments, progress, and site management.

Competing Interests: The authors declare no competing interests.

Figure Legends:

Fig.1 Illustration of the system principle and performance comparison. (a) Mechanism of generation for pure electronic microwave sources, including vacuum electronic devices (VEDs) and high electron mobility transistors (HEMTs). (b) Comparison of microwave source technology approaches. (c) Optoelectronic microwave source technology and its generation mechanism. (d) Comparison of output power and frequency tuning range between optoelectronic microwave sources and solid-state power amplifier microwave sources in the 0-2.5 GHz frequency band. (e) Comparison of the performance metrics of this study with existing optoelectronic devices. (f) Application domains and development directions of HPM sources. Icons used in this figure are sourced from Lucide and Feather under their respective open-source licenses.

Fig.2 System concept and architecture. (a) Conceptual schematic of the system. (b) Overall system architecture. LD: laser diode, Pre-AMP: pre-amplifier, EOM: electro-optic modulator, AOM: acousto-optic modulator.

Fig.3 Trade-off in material design between response speed and output amplitude. (a)The deep acceptor-shallow donor compensation mechanism and the electrical characteristics of SiC. E_a: acceptor energy level, E_c: conduction band energy level. (b) The impact of total response time on output voltage at different frequencies. (c) Comparison of response times between junction-type and photoconductive devices with a same conduction area: 4.5 mm². (d) Testing and fitting result of differential optical density (ΔOD) of Sample 1 and Sample 2. (e) Normalized output waveform and voltage–frequency characteristics under varying response times. (f) Output peak voltage across the 1–4 GHz band for different electron capture cross-sections. (g) Effect of increasing the

N/V doping concentration from 0.8×10^{17} / 2×10^{17} cm^{-3} to 1.2×10^{17} / 3×10^{17} cm^{-3}on output power under different load resistances.

Fig.4 Breakdown voltage and current-handling capability of the device. (a) Detail of the vertical-type device structure. (b) The electric field and current density distribution on the surface. (c) Dark-state breakdown waveform of the device and schematic of electrode edge damage. (d) Optical coupling structure. (e) Relationship between Al-doped ZnO (AZO) surface transmittance and film thickness, with an optical absorption coefficient (k) of 0.05. (f) Temporal evolution of total optical absorption as a function of incident intensity. (g) Variation of the device's output current amplitude with bias voltage and incident light energy. (h) Power capacity test results of the device under a bias voltage of 30 kV and a single-pulse light energy of 35 mJ. (i) Comparison of the maximum peak current and power capacity in the photoconductive device field.

Fig.5 The output of the OEMS. (a) Output waveforms at modulation frequencies of 0.5–1.5 GHz. (b) Frequency–power characteristic. (c) Frequency spectra of the output signal.

Fig.6 Array application of the OEMS. (a) Optical signal waveform within the measurement window. (b) Time interval error (TIE) sequence of the optical signal. (c) Modified phase-noise power spectrum $L(f)$. (d) Far-field measurement setup and physical diagram of the link. Icons used in this figure are sourced from Lucide and Feather under their respective open-source licenses. (e) Statistical values of the far-field amplitude for single-path and array radiation. (f) Radiation pattern of the array.

Editorial Summary

The authors showcase a fast-response silicon-carbide optoelectronic microwave source that delivers picosecond carrier-lifetime control and supports power handling up to 55 MW. It offers continuously tunable P–L-band pulses with >1 MW peak output over 0.25–1.3 GHz.

Peer review information: *Nature Communications* thanks the anonymous reviewer(s) for their contribution to the peer review of this work. A peer review file is available.

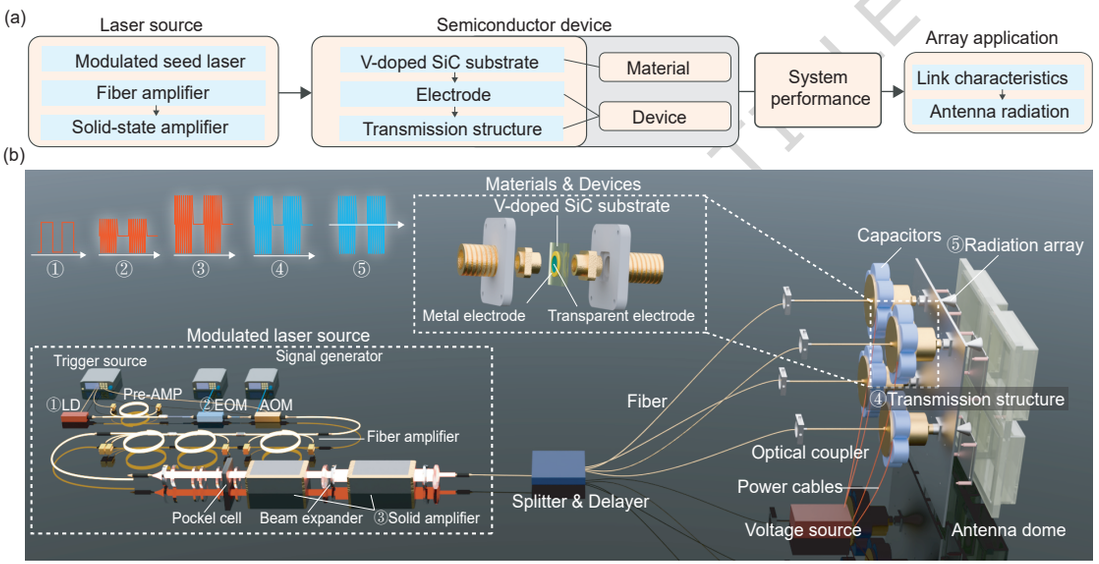

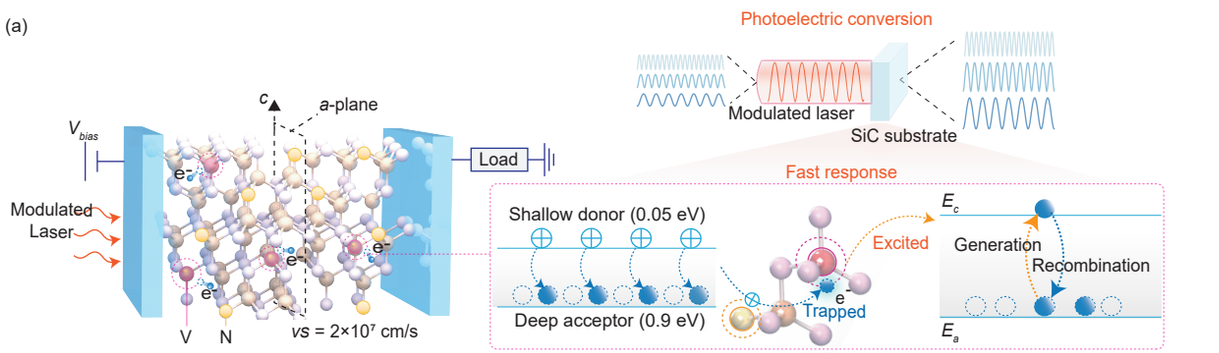

(b)

(d)

(f)